

Roche tomography of cataclysmic variables – IV. Starspots and slingshot prominences on BV Cen

C. A. Watson,^{1*} D. Steeghs,² T. Shahbaz,³ and V. S. Dhillon¹

¹ *Department of Physics and Astronomy, University of Sheffield, Sheffield S3 7RH, UK*

² *Harvard-Smithsonian Center for Astrophysics, 60 Garden Street, Cambridge, MA 02318, USA*

³ *Instituto de Astrofísica de Canarias, 38200 La Laguna, Tenerife, Spain*

Submitted for publication in the Monthly Notices of the Royal Astronomical Society

24 November 2018

ABSTRACT

We present Roche tomograms of the G5–G8 IV/V secondary star in the long-period cataclysmic variable BV Cen reconstructed from MIKE echelle data taken on the Magellan Clay 6.5-m telescope. The tomograms show the presence of a number of large, cool starspots on BV Cen for the first time. In particular, we find a large high-latitude spot which is deflected from the rotational axis in the same direction as seen on the K3–K5 IV/V secondary star in the cataclysmic variable AE Aqr. BV Cen also shows a similar relative paucity of spots at latitudes between 40–50° when compared with AE Aqr. Furthermore, we find evidence for an increased spot coverage around longitudes facing the white dwarf which supports models invoking starspots at the L_1 point to explain the low-states observed in some cataclysmic variables. In total, we estimate that some 25 per cent of the northern hemisphere of BV Cen is spotted.

We also find evidence for a faint, narrow, transient emission line with characteristics reminiscent of the peculiar low-velocity emission features observed in some outbursting dwarf novae. We interpret this feature as a slingshot prominence from the secondary star and derive a maximum source size of 75,000 km and a minimum altitude of 160,000 km above the orbital plane for the prominence.

The *entropy landscape* technique was applied to determine the system parameters of BV Cen. We find $M_1 = 1.18 \pm_{0.16}^{0.28} M_\odot$, $M_2 = 1.05 \pm_{0.14}^{0.23} M_\odot$ and an orbital inclination of $i = 53^\circ \pm 4^\circ$ at an optimal systemic velocity of $\gamma = -22.3 \text{ km s}^{-1}$. Finally, we also report on the previously unknown binarity of the G5IV star HD 220492.

Key words: stars: novae, cataclysmic variables – stars: spots – stars: late-type – stars: imaging – stars: individual: BV Cen – techniques: spectroscopic

1 INTRODUCTION

Cataclysmic variables (CVs) are short period binary systems in which a (typically) late main-sequence star (the secondary) transfers material via Roche-lobe overflow to a white dwarf primary star. For an excellent review of CVs, see Warner (1995). Although CVs are largely observed to study the fundamental astrophysical process of accretion, it is the Roche-lobe filling secondary stars themselves that

are key to our understanding of the origin, evolution and behaviour of this class of interacting binary.

In particular, the magnetic field of the secondary star is thought to play a crucial role in the evolution of CVs – driving CVs to shorter orbital periods through *magnetic braking* (e.g. Kraft 1967, Mestel 1968, Spruit & Ritter 1983, Rappaport, Verbunt & Joss 1983). Furthermore, the transition of the secondary star to a fully convective state and the supposed shutdown of magnetic activity that this transition brings is also invoked to explain the period gap – the dearth of CVs with orbital periods between ~ 2 –3 hours. On more immediate timescales, magnetic activity on the secondary

* E-mail: c.watson@sheffield.ac.uk

stars are also thought to explain variations in CV orbital periods, mean brightnesses, mean outburst durations and outburst shapes (e.g. Bianchini 1990; Richman et al. 1994; Ak et al. 2001).

That the secondary star and its magnetic field should have such a large and wide-ranging impact on CV properties should come as no surprise – the secondary star essentially acts as the fuel reserve that powers these binaries. Therefore, an understanding of the magnetic field properties of the secondary stars in CVs (e.g. spot sizes, distributions and their variation with time) is crucial if we are to understand the behaviour of these binaries. In addition, detailed studies of the rapidly rotating secondary stars in CVs can also provide tests of stellar dynamo theories under extreme conditions. For example, questions regarding the impact of tidal forces on magnetic flux tube emergence (e.g. Holzwarth & Schüssler 2003) and its effect on differential rotation (e.g. Scharlemann 1982) are particularly pertinent (see Watson, Dhillon & Shahbaz 2006 for a discussion).

Despite this, until recently there had been little direct observational evidence for magnetic activity in CVs. Webb, Naylor & Jeffries (2002) used TiO bands to infer the presence of spots on the secondary star in SS Cyg and estimated a spot filling factor of 22 per cent. Unfortunately, this technique does not allow the surfaces of these stars to be imaged and hence the spot distributions could not be ascertained.

Most recently, Watson et al. (2006) used Roche tomography to map the starspot distribution on a CV secondary (AE Aqr) for the first time. In Watson et al. (2006) we estimated that starspots covered approximately 18 per cent of the northern hemisphere of AE Aqr. The Roche tomogram of AE Aqr also showed that starspots were found at almost all latitudes, although there was a relative paucity of starspots at a latitude of $\sim 40^\circ$. Furthermore, we found that, in common with Doppler images of single rapidly rotating stars, AE Aqr also displayed a large high-latitude spot. In this work we continue our series of papers on Roche tomography (see Watson & Dhillon 2001, Watson et al. 2003, Watson et al. 2006) by mapping starspots on the long period (0.61-d) dwarf nova BV Cen for the first time. We also report on the serendipitous discovery of the binarity of HD220492.

2 OBSERVATIONS AND REDUCTION

Simultaneous spectroscopic and photometric observations were carried out over 3 nights on 2004 July 8–10. The spectroscopic data were acquired using the 6.5-m Magellan Clay Telescope and the simultaneous photometry was carried out using the Carnegie Institution’s Henrietta Swope 1.0-m Telescope. Both telescopes are situated at the Las Campanas Observatory in Chile.

2.1 Spectroscopy

The spectroscopic observations of BV Cen were carried out using the dual-beam Magellan Inamori Kyocera Echelle spectrograph (MIKE – see Bernstein et al. 2003). The MIT Lincoln Labs CCD-20 chip with 2046×4096 pixels was used in the blue channel, and the SiTe ST-002A chip, again with 2046×4096 pixels, was used in the red channel. The

standard setup was used, allowing a wavelength coverage of $3330\text{\AA} - 5070\text{\AA}$ in the blue arm and $4460\text{\AA} - 7270\text{\AA}$ in the red arm, with significant wavelength overlap between adjacent orders. With a slit width of 0.7 arcsec, a spectral resolution of around 38,100 ($\sim 7.8 \text{ km s}^{-1}$) and 31,500 ($\sim 9.5 \text{ km s}^{-1}$) was obtained in the blue and red channels, respectively. The chips were binned 2×2 resulting in a resolution element of ~ 2.3 binned pixels in the red arm and 2.6 binned pixels in the blue arm for our chosen slit. The spectra were taken using 400-s exposure times in order to minimise velocity smearing of the data due to the orbital motion of the secondary star. Comparison ThAr arc lamp exposures were taken every ~ 50 minutes for the purposes of wavelength calibration.

With this setup we obtained 63 usable spectra in each arm. Since the main goal of the Magellan run was to observe AE Aqr, we were restricted to 3-hour windows each night to observe BV Cen. Over our allocated 4 nights this would have allowed over 80 per cent of the orbit of BV Cen to be observed, but unfortunately we lost the final night due to bad weather. Other than that, the seeing was typically 0.6–0.7 arcsec on the first night and 0.9 arcsec on the next two nights, with occasional degradation to 1.5 arcsec. The peak signal-to-noise of the blue spectra ranged from 29 – 56 (typically ~ 50) in the blue arm, and from 38 – 76 (typically ~ 65) in the red arm. Table 1 gives a journal of the observations.

It should be noted that when using MIKE it is not possible to change the slit orientation on the sky. In order to compensate for this, and reduce atmospheric dispersion across the slit, MIKE is mounted at a 30° angle to the Naysmith platform. This means that at zenith distances greater than $\sim 50^\circ$ dispersion across the slit becomes significant. To avoid this, all observations of BV Cen were carried out at low airmasses and no exposure of BV Cen was carried out for an airmass above 1.39 (zenith distance $> 44^\circ$).

2.1.1 Data reduction

The data were reduced using the MIKE REDUX IDL pipeline version 1.7. This automatically processes all calibration frames and then wavelength calibrates, sky subtracts, flux calibrates and optimally extracts the target frames. The final output consists of 1-d spectra for the blue and red arms. The typical rms scatter reported for the wavelength calibration was around 0.002\AA . Since the REDUX package outputs vacuum wavelengths, whereas the linelists used in the Least Squares Deconvolution process (see Section 3) are measured in air, the wavelengths have been converted to air using the IAU standard given by Morton (1991).

Unfortunately, we experienced some flux calibration problems around regions of strong emission lines (e.g. H α and H β), most likely due to poor tabulation of our flux standard star HR 5501 around these lines. Since we mask out the strong emission lines during our study of the donor star absorption lines, this problem does not affect this work. We also found that we could not resolve (at the data reduction stage) a small jump in the flux level between the blue and red arms. We discuss the solution to this latter problem in Section 3.

Since the secondary star contributes a variable amount to the total light of a CV, Roche tomography is forced to use relative line fluxes during the mapping process (i.e. it is not possible to employ the usual method of normalising

Table 1. Log of the spectroscopic observations of BV Cen, the relevant spectral-type template stars, a telluric-correction star and the spectrophotometric standards HR 5501 and HR 9087. The first column gives the object name, columns 2–4 list the UT start Date and the exposure start and end times, respectively, and columns 5–6 list the exposure times and number of spectra taken for each object. The final column indicates the type of science frame taken and, where applicable, the measured systemic velocities, γ , of the template stars computed from Gaussian fits to their Least Squares Deconvolved profiles (see Section 5).

Object	UT Date	UT Start	UT End	T_{exp} (s)	No. spectra	Comments
HR 5501	2004 Jul 08	22:40	22:45	1–7	5	Spectrophotometric standard
BV Cen	2004 Jul 08	23:34	02:31	400	22	Target spectra
HR 9087	2004 Jul 09	10:07	10:13	1–4	6	Spectrophotometric standard
HR 5501	2004 Jul 09	22:40	22:49	1.5	12	Spectrophotometric standard
BV Cen	2004 Jul 09	23:42	02:21	400	20	Target spectra
Gl 863.3	2004 Jul 10	10:08	10:14	15–60	4	G5V template; $\gamma = +67.28 \pm 0.10$ km s ⁻¹
HD 221255	2004 Jul 10	10:25	10:42	20–100	5	G6V template; $\gamma = -11.55 \pm 0.10$ km s ⁻¹
HD 224287	2004 Jul 10	10:52	11:04	60–200	5	G8V template; $\gamma = +44.57 \pm 0.10$ km s ⁻¹
HR 5501	2004 Jul 10	22:41	22:47	1.5–8	8	Spectrophotometric standard
BV Cen	2004 Jul 10	23:35	02:18	400	21	Target spectra
HD 217880	2004 Jul 11	10:20	10:27	45–80	4	G8IV template; $\gamma = -67.24 \pm 0.10$ km s ⁻¹
HD 220492	2004 Jul 11	10:32	10:42	45–120	5	G5IV template; binary
BS 8998	2004 Jul 11	10:47	10:52	1.5–8	6	Telluric B9V star

the data). In order to determine these relative fluxes, the slit losses need to be calibrated. The standard technique of using a comparison star on the slit is, however, not possible with MIKE due to the tightly-packed, cross-dispersed format, and so simultaneous photometry is required (see Section 2.2). We corrected for slit losses by dividing each BV Cen spectrum by the ratio of the flux in the spectrum (after integrating the spectrum over the appropriate photometric filter response function) to the corresponding photometric flux (see Section 2.2). We should note here that the slit-loss correction factors were only calculated using the red spectra, but applied to both arms of the spectroscopic data. A further correction was applied to the blue arm (to account for both a different slit-loss factor in the blue compared to the red and also the jump in flux level between the two arms mentioned earlier) at the Least Squares Deconvolution stage (see Section 3).

2.2 Photometry

Simultaneous photometric observations were carried out using a Harris V-band filter and the Site3 CCD chip with 2048×3150 pixels. The CCD chip was windowed to a size of 633×601 pixels (which covered the target and the brightest comparison stars, as well as the bias strip) resulting in a $4' \times 4'$ window on the sky. Windowing allowed the readout time to be reduced to 46-s for each 15-s exposure on BV Cen.

2.2.1 Data reduction

The photometry was reduced using standard techniques. Since the master bias-frame showed no ramp or large scale structures across the chip, the bias level of the frames was removed by subtracting the median of the pixels in the over-scan regions. Pixel-to-pixel sensitivity variations were then corrected by dividing the target frames through by a master twilight flat-field frame. Optimal photometry was performed using the package PHOTOM (Eaton, Draper & Allen 2002).

There were two suitable comparison stars on each

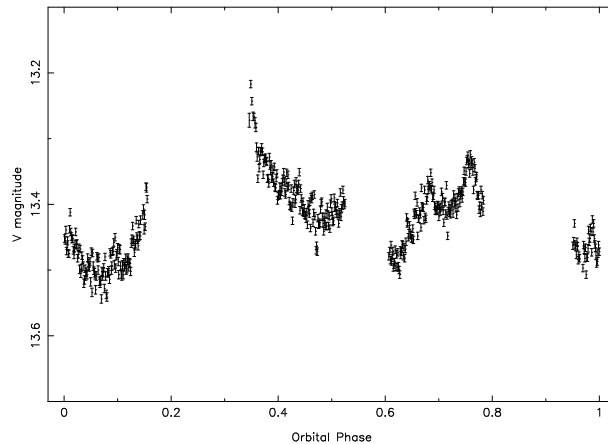


Figure 1. The V-band light curve of BV Cen. The data have been phased according to the ephemeris derived in Section 5. All 3 nights data have been plotted together from phase 0 – 1.

BV Cen target frame, identified from the ESO Guide Star Catalogue as GSC0866601471 (hereafter 1471) and GSC0866600859 (hereafter 0859). Two other bright stars in the field were deemed unsuitable since one was over-exposed, and the other had a nearby companion. Unfortunately, neither of the comparisons had reliable magnitude measurements available. We therefore used observations of the Landolt photometric standard SA105-437 to calibrate our instrumental magnitudes. This allowed us to determine the magnitude of 1471 and 0859 as $m_v = 13.43 \pm 0.07$ and $m_v = 13.54 \pm 0.07$, respectively. Finally, differential photometry was performed using the bright nearby comparison 1471. The light curve is shown in Fig. 1.

2.3 Continuum fitting

The continuum of the BV Cen spectra were fitted in exactly the same manner as that outlined in the Roche tomography study of AE Aqr (Watson et al. 2006). Spline knots

were placed at locations in the spectra that were relatively line-free. The spline knot positions were chosen on an individual spectrum-by-spectrum basis (though the locations of the knots were generally the same for each spectrum) until a smooth and visually acceptable fit was obtained. Again, as in Watson et al. (2006), we found that we systematically fit the continuum at too high a level, leading to continuum regions in the Least Squares Deconvolved (LSD – see Section 3) profiles lying below zero. The continuum fit was then shifted to lower levels until the continuum level in the LSD profiles lay at zero. The exact value of this shift varied from spectrum to spectrum, due to changes in the continuum shape as a result of variable accretion light, but the variation was generally small. We found that this process did not change the actual LSD profile shape.

3 LEAST SQUARES DECONVOLUTION

Least Squares Deconvolution (LSD) effectively stacks the ~ 1000 's of photospheric absorption lines observable in a single echelle spectrum to produce a 'mean' profile of greatly increased signal-to-noise. The technique of LSD is well documented and was first applied by Donati et al. (1997) and has since been used in many Doppler imaging studies (e.g. Barnes et al. 1998; Lister et al. 1999; Barnes et al. 2000; Barnes et al. 2001; Jeffers et al. 2002; Barnes et al. 2004; Marsden et al. 2005) as well as in the successful mapping of starspots on AE Aqr (Watson et al. 2006). For detailed information on LSD, see these references as well as the review by Collier Cameron (2001).

At present we use line lists generated by the Vienna Atomic Line Database (VALD – Kupka et al. 1999; Kupka et al. 2000) for LSD. The spectral type of the secondary star in BV Cen has been determined to lie within the range G5–G8 IV/V (Vogt & Breysacher 1980). In our analysis (see Section 5) later type spectral templates appear to fit the BV Cen spectra better, with our closest match being a G8IV template. In accordance with this, we downloaded a line-list for a stellar atmosphere with $T_{eff} = 5250$ K and $\log g = 3.55$ (the closest approximation available in the database to a G8IV spectral type). We do not consider a slight error in the choice of line-list used as having a significant impact on the results of the LSD process – see the discussion on this topic in Watson et al. (2006) and also Barnes (1999). Since this line-list contained normalised line-depths, whilst Roche tomography uses continuum-subtracted data, each line-depth has been multiplied by the corresponding value in a continuum fit to the G8IV template spectrum.

In order to circumvent the small flux 'jump' between the blue and red arms reported in Section 2.1.1, we carried out LSD in each arm separately. For the red arm, LSD was carried out over a wavelength range of $\sim 5050\text{\AA}$ to $\sim 6860\text{\AA}$, while for the blue arm the wavelength range was $\sim 4030\text{\AA}$ to $\sim 5050\text{\AA}$. Regions of strong emission lines such as $H\alpha$ and $H\beta$ were also masked out. Some 2790 lines were used in the deconvolution process across both arms, leading to a multiplex gain in signal-to-noise of ~ 22 and yielding absorption profiles with a signal-to-noise of ~ 1300 . Our version of LSD propagates the errors through the deconvolution process.

Since the red-spectra were slit-loss corrected using simultaneous photometry, the resulting LSD profiles from the

red data are scaled correctly relative to one-another. We then rebinned the blue LSD profiles to the same velocity scale as the red profiles (since the blue arm had a superior resolution) using sinc-function interpolation. Slit-loss corrections to the blue LSD profiles were then made by scaling the blue LSD profiles to match the red profiles obtained at the same phase. This scaling was done using an optimal subtraction algorithm. The blue profiles were scaled by a factor f and then subtracted from the red profile. The factor f that resulted in the minimum scatter in the residuals (compared to a smoothed version of the residuals) was then used to scale the blue LSD profiles. This method allowed the slit-losses in the blue to be calibrated despite the jump in flux between the red and blue arms. In addition, this method also allows further loss of light in the blue due to differential refraction to be corrected to first order. Deconvolving the blue and red data separately also allowed us to look for systematic problems and/or differences in the profiles, of which none were apparent. We should note, however, that the LSD profiles exhibit a slight tilt, with the red continuum (more positive velocities) systematically higher than the continuum on the other side of the profile. This is a well-known artefact (e.g. Barnes 1999) which will have little impact on the final image reconstruction.

The individual LSD profiles are shown in Fig. 2. These clearly show the distinct emission bumps due to starspots moving from blue (-ve velocities) to red (+ve velocities) through the profile as BV Cen rotates. When the LSD profiles are trailed (Fig. 3) these features are still obvious in addition to the secondary stars orbital motion and variations in the projected equatorial velocity, $v \sin i$. Fig. 3 also shows the trailed LSD profiles after removal of the orbital motion and subtraction of a theoretical profile at each phase. The theoretical profiles were calculated using our Roche tomography code by adopting the binary parameters and limb darkening described in Section 6 and a featureless stellar disc. This process increases the contrast and enhances the starspot signatures (which now appear dark).

4 ROCHE TOMOGRAPHY

Roche tomography is analogous to Doppler Imaging (e.g. Vogt & Penrod 1983) and has now been successfully applied to the donor stars of CVs on several occasions (Rutten & Dhillon 1994; Rutten & Dhillon 1996; Watson et al. 2003; Schwöpe et al. 2004; Watson et al. 2006). Rather than repeat a detailed description of the methodology and axioms of Roche Tomography here, we refer the reader to the references above and the technical reviews of Roche Tomography by Watson & Dhillon (2001), Dhillon & Watson (2001) and Watson & Dhillon (2004). The pertinent points with respect to this work are that we employ a moving uniform default map, where each element is set to the average value of the reconstructed map. Furthermore, we do not adopt a two-temperature or filling factor model (e.g. Collier Cameron & Unruh 1994), since these assume only two temperature components across the star while CV donors are expected to exhibit large temperature differences due to the impact of irradiation. This means our Roche tomograms may be prone to the growth of bright pixels

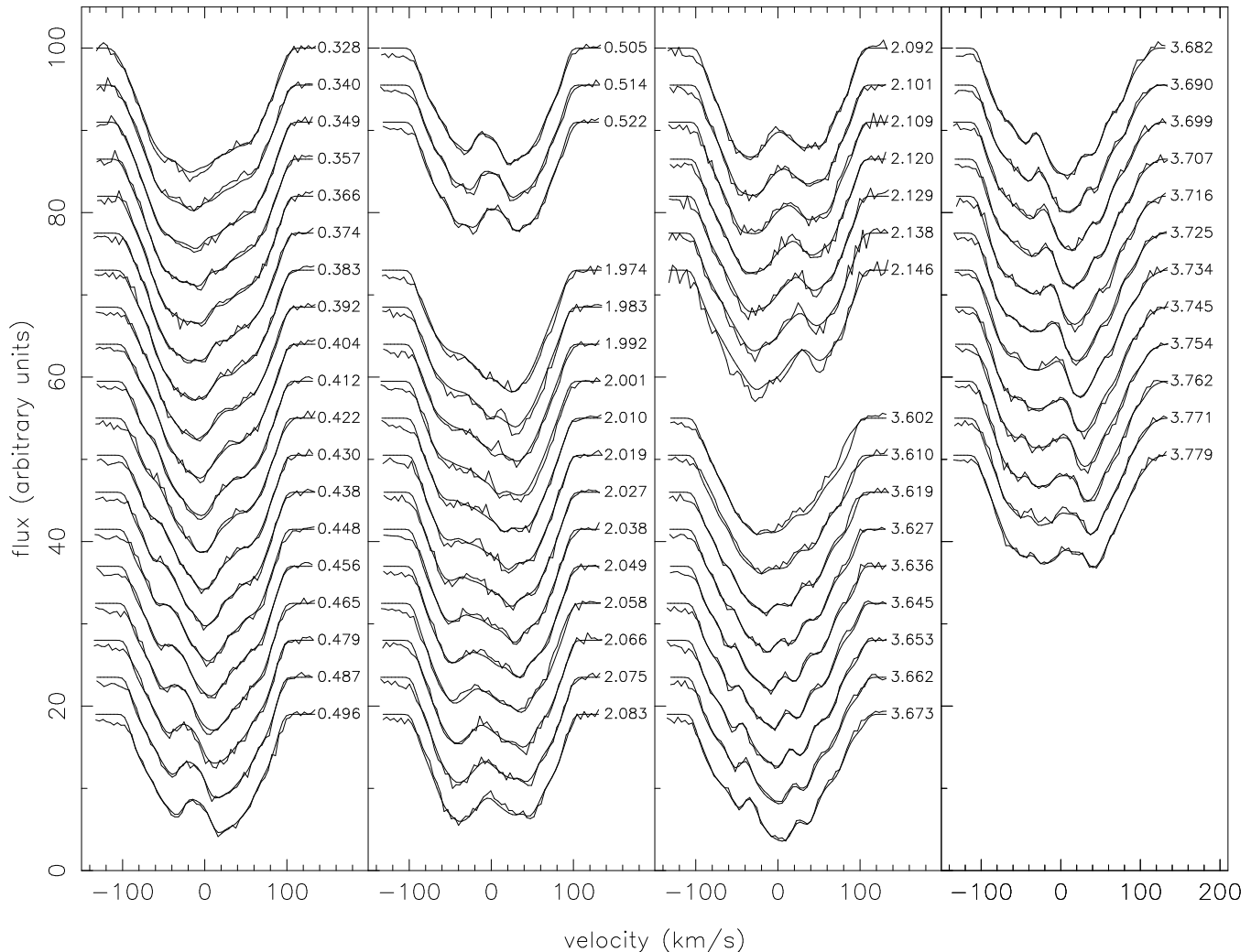


Figure 2. The LSD profiles and maximum entropy fits (see Section 7 for further details) for BV Cen. The velocity of the secondary star has been removed using the parameters found in Section 6, and each profile is shifted vertically for clarity. The orbital phase for each exposure is indicated at the top right of each profile.

(which two-temperature models suppress, Collier Cameron 1992) and are quantitatively more difficult to analyse.

5 EPHEMERIS

5.1 Ephemeris

Despite the brightness of BV Cen, and the fact that it is one of the longest period dwarf novae known, the system has been poorly studied. The most recent orbital ephemeris for BV Cen was published by Gilliland (1982) and will have accumulated a large error over the last two decades. We have therefore determined a new ephemeris for BV Cen by cross-correlation with suitable template stars that were observed using the same instrumental setup. The cross-correlation was carried out over the spectral range $6400\text{\AA} - 6536\text{\AA}$. This wavelength range not only covers several moderately strong lines and blends from the secondary that are useful for radial velocity measurements but include several temperature and gravity sensitive lines for F–K stars (Strassmeier & Fekel 1990).

The BV Cen and template spectra were first rebinned onto the same velocity scale using sinc-function interpolation and then normalised by dividing through by a constant. The continuum was then subtracted by a 3rd order polynomial fit. This procedure is followed to ensure that the line strengths are preserved across the spectral region of interest. The template spectra were then broadened to account for the rotational velocity ($v \sin i$) of the secondary star – the amount of broadening applied was determined using an optimal-subtraction technique. In this method the template spectra were first broadened by an arbitrary amount before being cross-correlated against the BV Cen spectra, allowing a first iteration on the radial velocity curve of BV Cen. The BV Cen data were then orbitally-corrected using the results of this radial velocity analysis and averaged. The template spectra were once more broadened by different amounts in 0.1 km s^{-1} steps, multiplied by a constant, f , and then subtracted from the orbitally-corrected mean BV Cen spectrum. The broadening that gave the minimum scatter in the residual optimally-subtracted spectrum was then applied to the template spectrum and the whole procedure repeated

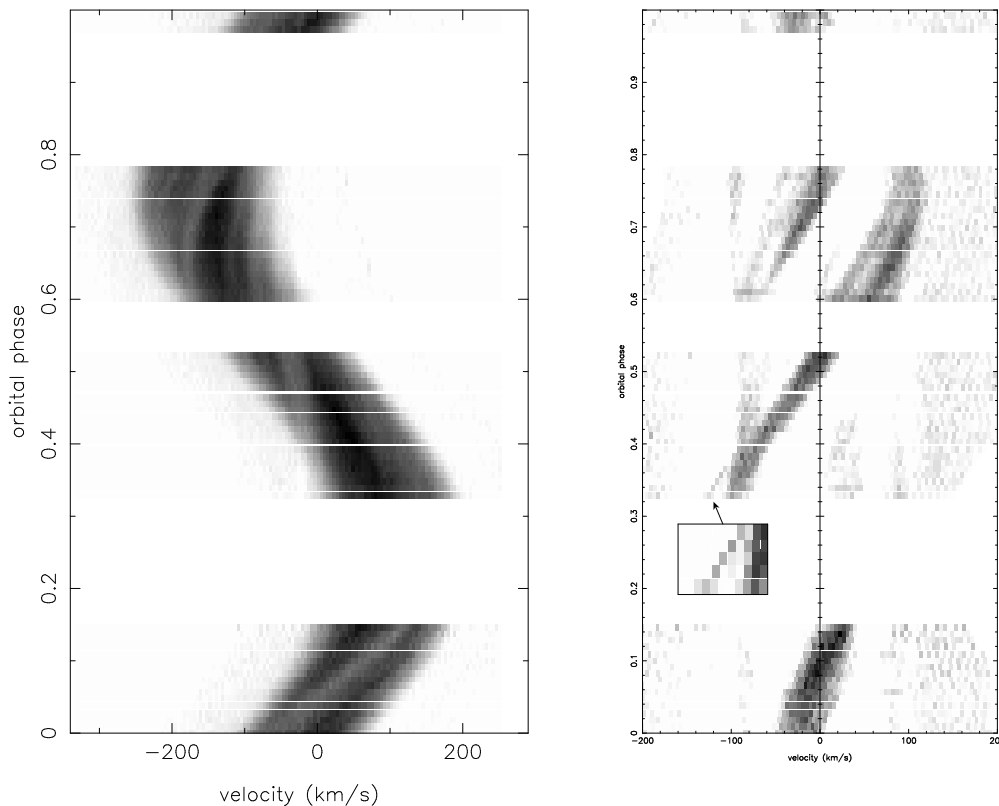


Figure 3. Left-hand panel: A trail of the deconvolved profiles of BV Cen. The large gaps are due to non-continuous observations over three nights. The small gaps in the phase coverage are at times when arc spectra were taken for the purpose of wavelength calibration. Features due to starspots appear bright and several such features are clearly visible traversing the profiles from blue (more -ve velocities) to red (more +ve velocities) in the trailed spectra. Also evident is the orbital motion and variation in $v \sin i$, which shows a maximum at phase 0.75 due to the varying aspect of the tidally distorted secondary star. Right-hand panel: The same as the left-hand panel, except the orbital motion has been removed using the binary parameters derived in Section 6. This allows the starspot tracks across the profiles to be more easily followed. In order to increase the contrast of this plot, we have subtracted a theoretical profile (see text) from each LSD profile before trailing. Features due to starspots and irradiation appear dark in these plots. Note the narrow feature (indicated with an arrow and shown enlarged – see inset) that lies outside the blue edge of the profiles at phases 0.328–0.366, which seems to follow the motion of the large feature that runs through the profiles during this block of observations. This feature is discussed in more detail in Section 8.

until the rotational broadening value no longer changed. This typically took 2 or 3 iterations.

Through the above process a cross-correlation function (CCF) was calculated for each BV Cen spectrum. A radial velocity curve can then be derived by fitting a sinusoid through the CCF peaks. Unfortunately, none of our spectral-type templates provided a good match to the BV Cen spectra, all requiring a multiplication factor $f > 1$, which would imply that the secondary star contributes more than 100 per cent of the system light. We also discovered that our G5IV template star HD220492 is actually a close binary (see Section 5.2).

Fortunately, as discussed in Watson et al. (2006), the CCFs calculated are insensitive to the use of an ill-matching spectral template and, despite requiring multiplication factors $f > 1$, the broadened template spectra still provided visually acceptable matches to the orbitally corrected BV Cen spectrum. The radial velocity curve in Fig. 4 was obtained after cross-correlation of the BV Cen spectrum with the G8IV star HD 217880 (our best guess spectral type for BV Cen). This allowed us to obtain a new zero-point for the ephemeris of

$$T_0 = \text{HJD } 2453195.2859 \pm 0.0003 \quad (1)$$

with the orbital period fixed at $P = 0.611179$ d (from Gilliland 1982). This ephemeris was applied to the rest of the data presented in this paper.

Cross-correlation with the G8IV template yielded a secondary star radial velocity amplitude of $K_r = 137.3 \pm 0.3$ km s⁻¹, a systemic velocity of $\gamma = -20.3 \pm 0.2$ km s⁻¹ and a rotational broadening $v \sin i = 95.3$ km s⁻¹ (see Section 6 for a discussion of the binary parameters). These values were consistent within 2 km s⁻¹ for all the spectral-type templates used. Since some of our spectral-type templates (including the G8IV template star HD 217880) did not have measured systemic velocities, we carried out least squares deconvolution (see Section 3) on each template star. The systemic velocity was then measured using a Gaussian fit to the sharp LSD profile, the results are listed in the final column of Table 1. We note that Gl 863.3 has a published systemic velocity ($+66.9 \pm 0.1$ km s⁻¹; Nordström et al. 2004) which is close to our measured value of $+67.28 \pm 0.10$ km s⁻¹ using this technique.

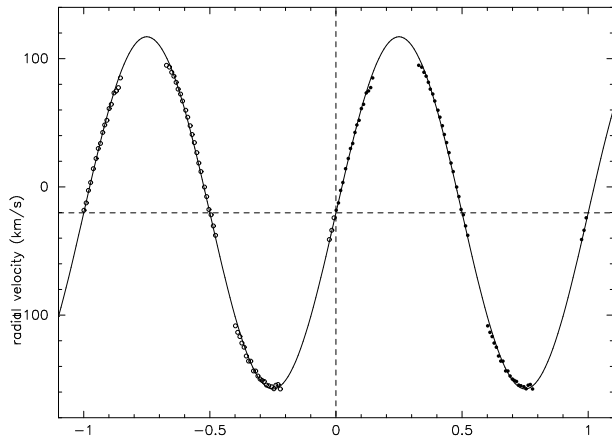


Figure 4. The measured secondary star radial-velocities with a sinusoidal fit from cross-correlation using a G8IV spectral-type template star. The data have been phase folded using the zero-point of Section 5. The error bars are typically smaller than the symbol size.

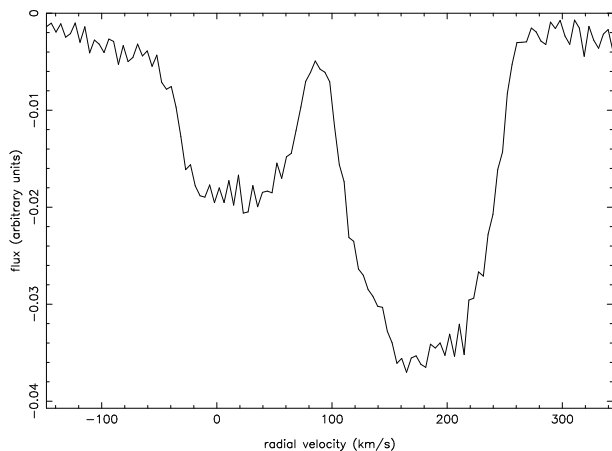


Figure 5. The LSD profile of HD220492. This system is most likely a close binary system containing an early to mid G-type star and a later type companion.

5.2 The binarity of HD220492

While measuring the systemic velocities of the spectral-type templates, we discovered that the G5IV spectral-type template HD 220492 is a close binary system. The LSD profile of this system is shown in Fig. 5 and clearly shows two heavily broadened stellar line profiles. It is most likely that this is a close binary system containing an early to mid G-type star and later-type companion. We note that the binary nature of HD 220492 was missed by the Geneva-Copenhagen survey of the Solar neighbourhood, since no radial velocity measurements of this star appear to have been taken (Nordström et al. 2004). HD 220492 is also listed as the optical counterpart to the X-ray source 1RXJS232426.0-450906 (Schwope et al. 2000), and was identified as a suspected variable star by Samus et al. (2004). Given the large $v \sin i$ and hence rapid rotation of these stars, both components are likely to be magnetically active. Unfortunately, since only 4 spectra over 7 minutes were taken, nothing can be said about the orbital period of this system.

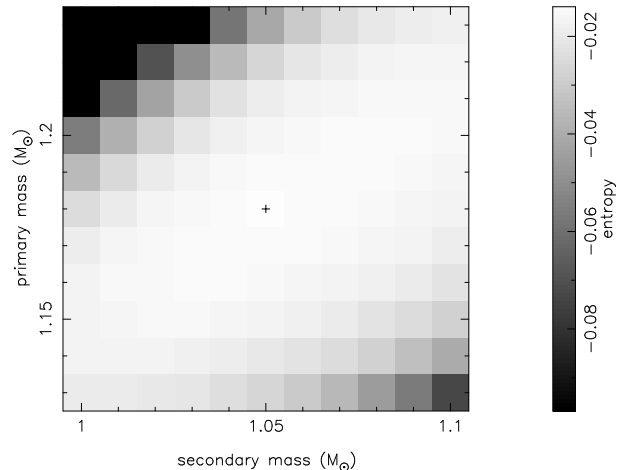


Figure 6. The entropy landscape for BV Cen, assuming an orbital inclination of $i = 53^\circ$ and a systemic velocity of $\gamma = -22.3 \text{ km s}^{-1}$. Dark regions indicate component masses for which no fit to the target χ^2 could be found. The cross marks the position of maximum entropy, corresponding to component masses of $M_1 = 1.18 M_\odot$ and $M_2 = 1.05 M_\odot$.

6 SYSTEM PARAMETERS

The system parameters (systemic velocity γ , orbital inclination i , secondary star mass M_2 and primary star mass M_1) of BV Cen have been determined using the same method as described in Watson et al. (2006). In short, adopting the incorrect parameters causes artefacts to appear in the Roche tomograms leading to an increase in the structure (and hence a decrease in the entropy) of the final image. This can be visualised as an *entropy landscape* (see Fig. 6), in which reconstructions to the same χ^2 are carried out for different combinations of component masses and the entropy obtained for each set plotted on a grid of M_1 versus M_2 .

In order to search for the correct set of parameters we have constructed a series of entropy landscapes for different inclinations and systemic velocities. This is done in an iterative manner by first constructing entropy landscapes for a sequence of systemic velocities for a fixed inclination. The optimal systemic velocity found in this first iteration was then fixed and a series of entropy landscapes were then calculated out over a range of orbital inclinations. Once an optimal orbital inclination was determined another sequence of entropy landscapes was carried out over a range of systemic velocities to ensure that the optimal systemic velocity had not changed. As we have found previously (Watson et al. 2003; Watson et al. (2006)), the systemic velocity obtained in this way is largely independent of the orbital inclination assumed in the reconstructions.

For the reconstructions of BV Cen we have adopted a root-square limb-darkening law of the form

$$I(\mu) = I_0 [1 - a_\lambda (1 - \mu) - b_\lambda (1 - \sqrt{\mu})] \quad (2)$$

where $\mu = \cos \gamma$ (γ is the angle between the line of sight and the emergent flux), I_0 is the monochromatic specific intensity at the center of the stellar disc, and a_λ and b_λ are the limb-darkening coefficients at wavelength λ . We calculated an effective central wavelength of 5067Å for our spectroscopic observations using

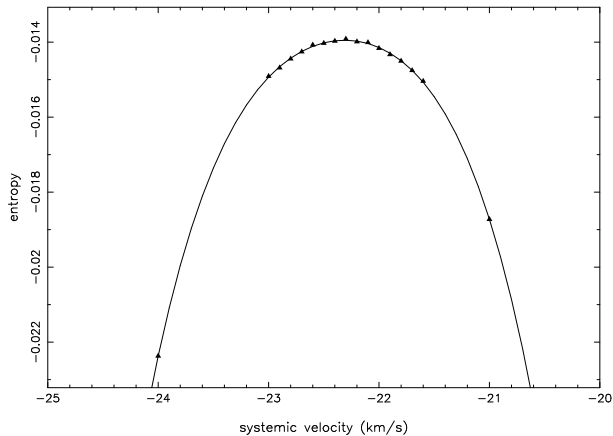


Figure 7. Points show the maximum entropy value obtained in each entropy landscape as a function of systemic velocity, assuming an orbital inclination of 53° . The solid curve is a 5th order polynomial which is only shown to emphasise the trend between entropy and systemic velocity. The highest data point corresponds to a systemic velocity of $\gamma = -22.3 \text{ km s}^{-1}$.

$$\lambda_{cen} = \frac{\sum_i \frac{1}{\sigma_i^2} d_i \lambda_i}{\sum_i \frac{1}{\sigma_i^2} d_i}, \quad (3)$$

where d_i and σ_i are the line-depths and error on the observed data at wavelength position λ_i , respectively. This, therefore, takes into account the line depths and noise in the spectrum. Limb-darkening coefficients for a star of $T_{eff} = 5250 \text{ K}$ and $\log g = 3.5$ (corresponding to a G8IV star – Dall et al. 2005) were obtained from Claret (1998) for the B- and V-bands. The values of the coefficients at these wavelengths were then linearly interpolated over to find $a=0.5388$ and $b=0.3088$ for the effective central wavelength of our observations. These coefficients were used for all the reconstructions carried out for this paper.

Fig. 7 shows the peak entropy value obtained in entropy landscapes constructed assuming an orbital inclination of $i=53^\circ$ (this value was obtained after carrying out the iterative procedure described above) but varying the systemic velocity. This yielded an optimal value of $\gamma = -22.3 \text{ km s}^{-1}$. We cannot assign a rigorous error estimate to the systemic velocity but we found that the image quality depended heavily on the assumed systemic velocity, and reconstructions were almost impossible for assumed systemic velocities that differed by more than $\pm 2 \text{ km s}^{-1}$ from the optimal value. Indeed, for this reason we sampled the systemic velocity more finely than for AE Aqr (Watson et al. 2006), incrementing in 0.1 km s^{-1} steps. It is unlikely, therefore, that the error on the systemic velocity exceeds $\pm 1 \text{ km s}^{-1}$ and is probably less than this.

Our value of $\gamma = -22.3 \text{ km s}^{-1}$, while close to the value of $\gamma = -20.3 \pm 0.2 \text{ km s}^{-1}$ derived from the radial velocity analysis performed in Section 5, is in stark contrast to the two previous published values known to us. These are $-47 \pm 10 \text{ km s}^{-1}$ (Vogt & Breysacher 1980) and $-47 \pm 2 \text{ km s}^{-1}$ (Gilliland 1982). We are uncertain as to the cause of this discrepancy. It is unlikely that surface inhomogeneities, such as those caused by irradiation from the accretion regions (and which is known to cause systematic errors in radial velocity measurements – e.g. Davey & Smith 1992; Watson et al.

2003), could cause this discrepancy. First, our systemic velocity derived from radial velocity analysis only differs from that derived from the entropy landscape method by 2 km s^{-1} , which implies that inhomogeneities on the surface of BV Cen have little impact. Second, one could argue that during the observations of Vogt & Breysacher (1980) and Gilliland (1982) the impact of irradiation may have been much greater. In the case of HU Aqr, which is heavily irradiated, we found that the systemic velocity measured by standard radial velocity analyses could be shifted by as much as -14 km s^{-1} from the true value (Watson et al. 2003). Such a shift, if applicable to BV Cen, would bring the results of Gilliland (1982) and Vogt & Breysacher (1980) into closer agreement with ours but only if a large portion of the leading hemisphere (the side of the star as seen from $\phi = 0.75$) was irradiated during their observations. The lightcurve of Vogt & Breysacher (1980) does indicate that the system was slightly brighter during their observations, but the system was certainly not in outburst and we would not expect a large amount of irradiation of the donor star. Furthermore, looking at our Roche tomograms in Section 7, irradiation of BV Cen appears to be fairly low, and certainly not large enough to impact a radial velocity curve analysis to the extent needed to bring our values of the systemic velocity into agreement. Nor do we believe that our wavelength calibration is incorrect, as we have measured the systemic velocity of Gl 863.3 using LSD and found it to be in agreement with Nordström et al. (2004) to within 0.4 km s^{-1} (see Section 5). Therefore, we have no satisfactory explanation of the discrepancy between our measured systemic velocity and those of Vogt & Breysacher (1980) and Gilliland (1982).

Fig. 8 shows the maximum entropy values as a function of the orbital inclination assuming the systemic velocity of $\gamma = -22.3 \text{ km s}^{-1}$ derived earlier. This shows a clear trend with the best fitting inclination at $i = 53^\circ$ which we have adopted as the optimal value for BV Cen. This value is lower than (but agrees to within $2\text{-}\sigma$) the orbital inclinations of $62^\circ \pm 5^\circ$ and $61^\circ \pm 5^\circ$ of Gilliland (1982) and Vogt & Breysacher (1980), respectively.

The entropy landscape for BV Cen carried out with $i = 53^\circ$ and $\gamma = -22.3 \text{ km s}^{-1}$ is shown in Fig. 6. From this we derive optimal masses for the white dwarf and secondary star of $M_1 = 1.18 M_\odot$ and $M_2 = 1.05 M_\odot$, respectively. These values for the binary parameters seem to fall in between the previously published ones. Vogt & Breysacher (1980) also find relatively high masses for the binary components of $M_1 = 1.4 \pm 0.2$ and $M_2 = 1.4 \pm 0.2$. Indeed, their derived white dwarf mass places it uncomfortably close to the Chandrasekhar limit while our new estimate lies more comfortably within the allowed mass limit for white dwarfs. On the other-hand, Gilliland (1982) find lower masses of $M_1 = 0.83 \pm 0.1$ and $M_2 = 0.9 \pm 0.1$. These masses, however, lead to a high mass ratio ($q = M_2/M_1$) of $q = 1.08 \pm 0.18$, which places BV Cen near the critical mass ratio for mass transfer instability (Politano 1996; Thoroughgood et al. 2004). Our higher secondary star mass, and lower mass ratio ($q = 0.89$) moves BV Cen comfortably within the region where mass transfer is stable. We should note that, since the optimal inclination we find is quite low, a small error in the derived inclination leads to quite a large error in the masses. As expected, we find that the optimal masses in our entropy landscapes vary as $\sin^3 i$.

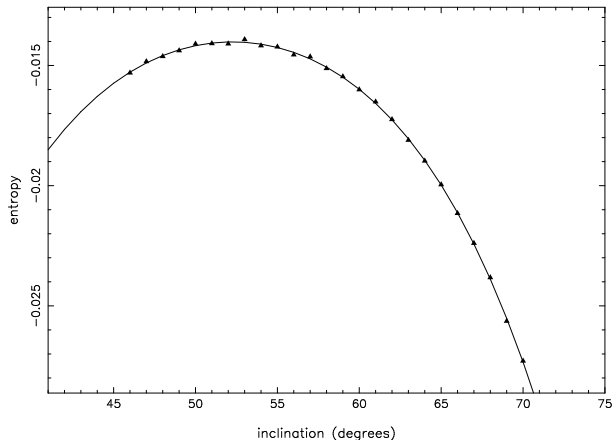


Figure 8. Points show the maximum entropy value obtained in each entropy landscape for different inclinations, assuming a systemic velocity of $\gamma = -22.3 \text{ km s}^{-1}$. The solid curve is a fifth order polynomial fit showing the general trend. The entropy value peaks at an orbital inclination of $i=53^\circ$. Inclinations lower than 49° result in an optimal white dwarf mass greater than the Chandrasekhar limit and so we have not been extended the analysis to significantly lower inclinations.

Selection of the correct χ^2 to aim for during the reconstructions is somewhat subjective. We select the χ^2 which results in a close fit to the data (all reconstructions were carried out to $\chi^2=2.5$, which indicates that our propagated errors are underestimated but this does not impact the final reconstructions), but not so close as to cause the Roche tomograms to break up into noise. In order to determine how robust the derived parameters are, we have explored the effects that changing the aim χ^2 has on the entropy landscapes. We find that fitting more closely to the data causes the maps to start to break up into noise, but we find that the derived inclination is the same ($i = 53^\circ$), and the masses for each entropy landscape are typically within $\pm 0.02 M_\odot$, and we never see a difference greater than $\pm 0.04 M_\odot$ for any assumed inclination. The same is true if we raise the aim χ^2 (poorer fit to the data), except we lose sensitivity to the inclination. Despite this, even fitting to substantially higher χ^2 's where the maps become featureless we still find a preference for inclinations between $\sim 52 - 60^\circ$. We are therefore confident in the robustness of our derived binary parameters.

Calculating the errors on our derived parameters is difficult. One could perform a series of Monte Carlo simulations of the data and carry out entropy landscape reconstructions for each synthetic dataset. Unfortunately, this would require a large amount of time to complete. Instead we can determine a rough guide to the errors from the scatter in the $v_{\text{sin}i}$ and K_r values obtained from conventional analysis of the data using the spectral-type templates described in Section 5. We found that the scatter in the measured K_r and $v_{\text{sin}i}$ values were, in both cases, $\pm 2 \text{ km s}^{-1}$. This leads to an error on the mass ratio, q , of ± 0.04 – which in turn translates into an error on the component masses of $\pm 0.03 M_\odot$. Such an error agrees with the scatter we find in the optimal values returned from entropy landscapes constructed for different χ^2 's. This then gives optimal parameters of $M_1 = 1.18$

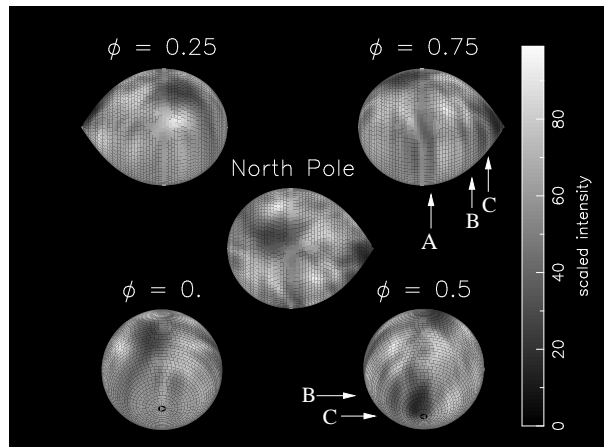


Figure 9. The Roche tomogram of BV Cen. Dark grey-scales indicate the presence of either star-spots or irradiated zones. The system has been plotted as the observer would see it at an orbital inclination of 53° , except for the central panel which shows the system as viewed from above the North Pole. The orbital phase (with respect to the ephemeris of Section 5) is indicated above each panel. For clarity, the Roche tomograms are shown excluding limb darkening. Individual spots referred to in the text are arrowed.

$\pm 0.03 M_\odot$ and $M_2 = 1.05 \pm 0.03 M_\odot$ at an inclination of 53° .

Clearly, the errors in the masses are dominated by any error in the derived orbital inclination. Again, we can make a conservative estimate to the likely error in our orbital inclination. A lower limit of $i = 49^\circ$ is set by the necessity that the white dwarf mass be lower than the Chandrasekhar limit. If we assume that, therefore, our inclination is accurate to $i=53 \pm 4^\circ$, we find $M_1 = 1.18 \pm_{0.16}^{0.28} M_\odot$ and $M_2 = 1.05 \pm_{0.14}^{0.23} M_\odot$.

7 SURFACE MAPS

Using the parameters derived in Section 6 we have constructed a Roche tomogram of the secondary star in BV Cen (see Fig. 9). The corresponding fit to the data are displayed in Fig. 2. A number of dark starspots are visible in the Roche tomogram. The most conspicuous of these is the high latitude spot (common in Doppler images of rapidly rotating stars) at a latitude of $\sim 65^\circ$. Such high-latitude spots seen on rapidly rotating stars are commonly believed to be caused by strong Coriolis forces acting to drive magnetic flux tubes towards the poles (Schüssler & Solanki 1992). This spot is also similar to the large high-latitude spot seen on AE Aqr by Watson et al. (2006), not just in its latitude but also in the way that it appears towards the trailing hemisphere of the star. If such a shift in high latitude spots on CV donor stars is common then this hints that a mechanism is in operation that drives flux-tube emergence to this side of the star. We discuss this in more detail later.

Also prominent is a dark feature near the L_1 point. Although it is possible that this may be due to a large spot (with obvious consequences for theories that invoke starspots to quench mass transfer), we have to consider that the secondary stars in CVs are located close to an irradiating

source (the bright spot and/or white dwarf, for example). It is well known that the inner face of the secondary, and the L_1 point in particular, is often irradiated. Indeed, early single-line Roche tomography studies of CVs concentrated on mapping the so-called irradiation patterns on the inner faces of the secondaries in CVs (e.g. Watson et al. 2003). While it is largely the contrast between the immaculate photosphere and lower spotted continuum contributions that cause spots to appear dark on our tomograms, irradiation causes the absorption lines to weaken due to ionisation and hence also appears dark.

We believe that the feature near the L_1 point in BV Cen is indeed due to irradiation. This interpretation is supported by the modelling of B–V lightcurves by Vogt & Breysacher (1980) who found evidence for a slightly enhanced temperature around the inner Lagrangian point. Gilliland (1982) also found evidence for a slightly heated inner face. Close inspection shows that the irradiation pattern is asymmetric, with the impact of irradiation strongest towards the leading hemisphere. This is very similar to the irradiation pattern seen on the dwarf-nova IP Peg (see Watson et al. 2003 and Davey & Smith 1992) which has been explained by irradiation from the bright spot which is located on the correct side of the star to create this asymmetry. Certainly the lightcurves of BV Cen (e.g. Vogt & Breysacher 1980) show a prominent bright spot component. Also Vogt & Breysacher (1980) suggested that the B–V variations could be explained if a small region of the star nearest to the gas stream and bright spot had a temperature excess of $\Delta T \sim 300$ K. The location of this heated region described by Vogt & Breysacher (1980) matches what we observe in the Roche tomogram.

Several other features in the Roche tomogram are also worth mentioning. One of these is a mid-latitude spot best seen at phase $\phi = 0.75$ (marked as spot A on Fig 9), which we have mentioned as it is one of the largest spots, other than the polar spot. Interestingly, there also seem to be two low-latitude spots near the L_1 point (spots ‘B’ and ‘C’ on Fig 9), but located on the leading hemisphere. Although these spots are fairly heavily smeared in latitude, they may be located at a sufficiently low latitude to cross the mass-transfer nozzle. It has been suggested that starspots are thought to be able to quench mass transfer as they pass the mass-losing nozzle on the donor, resulting in the low-states observed in many CVs (see Livio & Pringle 1994; King & Cannizzo 1998). The observations of low-latitude starspots near the L_1 point lends some credence to these models – it seems apparent that sizeable starspots, which are often seen at high latitudes on rapidly-rotating stars, can also form at low latitudes near the L_1 point in binaries.

It is unlikely that the spots we have identified near the L_1 point are, instead, due to irradiation. This would imply that the irradiation is patchy in nature (rather than smoothly varying across the stellar surface) in order to form the dark spots we observe in the tomogram. This, in turn, would require that the irradiation is either beamed towards relatively small patches on the stellar surface, or would require a complex accretion structure shielding the majority of the stellar surface and only allowing small spot-like regions to be irradiated. We can think of no reason why the irradiation should be beamed in this manner, nor why such a complex accretion structure should exist. In addition, while the limb-darkening around the L_1 region could be incorrect

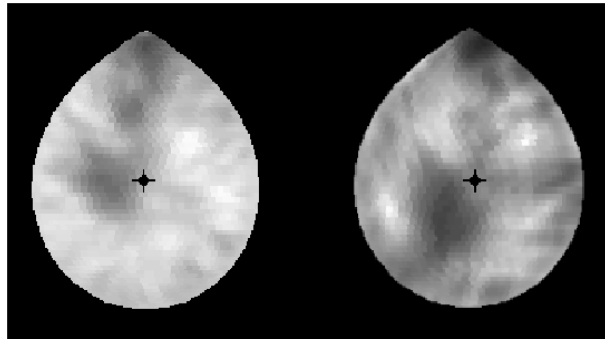


Figure 10. Roche tomograms of the donor stars in AE Aqr (left – from Watson et al. 2006) and BV Cen (right) as viewed from above the pole (indicated with a cross). Both show a high latitude spot displaced towards the left-most (trailing) hemisphere (the orbital motion is towards the right). Furthermore, both appear to show a chain of spots descending from the polar spot towards the L_1 point.

by a significant degree due to the low effective-gravity, again this would be a smoothly varying artifact and would not lead to dark spots on the Roche tomogram.

We also note that, when viewed from above the North pole of the star, there seems to be quite a distinct ‘chain’ of spots. This chain leads down from the polar regions towards the L_1 point, showing a possible deflection towards the leading hemisphere with decreasing latitude. In Fig. 10 we plot an enlarged polar view of both BV Cen and AE Aqr (from Watson et al. 2006) which shows more clearly these features. Comparison with the Roche tomogram of AE Aqr shows a similar distribution of spots (we make a more detailed comparison in Section 9). The fact that we see this same ‘chain’ of spots is suggestive of a mechanism that is forcing magnetic flux tubes to preferentially arise at these locations. Given that this is on the side of the star facing the white dwarf, this may be due to the impact of tidal forces which is thought to be able to force spots to arise at preferred longitudes (Holzwarth & Schüssler 2003). In a recent Doppler Image of the pre-CV V471 Tau, Hussain et al. (2006) also found the presence of high-latitude spots located on the side of the star facing the white dwarf.

In addition to the features outlined above, a number of other small spots are visible. We have examined the intensity distribution of the pixels on our Roche tomogram in order to make a more quantitative analysis of the spot distribution. In our Roche tomography study of AE Aqr (Watson et al. 2006), we looked for a bimodal distribution in pixel intensities and labelled the population of lower intensity pixels as spots, and higher intensity pixels as immaculate photosphere. Unfortunately, unlike AE Aqr, BV Cen does not show a clear bimodal distribution in pixel intensities from which we can confidently distinguish between immaculate and spotted photosphere (note that we neglected regions that are not visible and therefore have pixel intensities set to the default value). Instead, the histogram of pixel intensities shows a broad peak, with long tails towards high and low pixel intensities. We have therefore defined a spot intensity by examining the polar spot feature. At the centre of the polar spot, the pixel intensities are very stable, and we have taken the intensity of the central regions of the polar

spot to represent the intensity of a 100% spotted region. Although there are lower intensity pixels present in the Roche tomogram (which contribute to the tail of low intensity pixels in the maps), all of these were found to be confined to the irradiated zone near the L_1 point. (We should note that the fact that the region around the L_1 point has pixel intensities quite different from those of the spotted regions supports our interpretation that this feature is not a spot). We are therefore reasonably confident in our identification of the spotted regions on BV Cen.

Determining the immaculate photosphere was somewhat more difficult. There appear to be some bright regions in the map, especially near the polar spot. It is unlikely that these represent the immaculate photosphere; the growth of bright pixels in maps that are not ‘thresholded’ is a known artifact of Doppler imaging methods (e.g. Hatzes & Vogt (1992) – also see Section 4), and it is likely that these features are due to this, contributing to the long tail of bright pixel intensities that we see. Instead, we have selected the intensity at the upper end of the broad peak of pixel intensities in the histogram to represent the immaculate photosphere. If we assume that the appearance and disappearance of spots simply alters the continuum level (and not the line-depths, which has a secondary influence on the LSD profiles) and a blackbody scaling, this gives a temperature contrast between the photosphere and spot of $\Delta T = 780\text{K}$. Such a temperature difference seems reasonable. From simultaneous modelling of lightcurves and line-depth ratios of three active RS CVn systems, Frasca et al. (2005) found a temperature difference between spotted and immaculate photosphere of $\Delta T = 450\text{--}850\text{ K}$. Similarly, Biazzo et al. (2006) find temperature differences of $\Delta T = 453\text{--}1012\text{K}$ for stars at different locations along the HR diagram, with stars of lower surface gravity having spots with a lower ΔT .

Each pixel in our Roche tomogram was given a spot-filling factor between 0 (immaculate) to 1 (totally spotted) depending on its intensity between our predefined immaculate and spotted photosphere intensities. After removal of the region near the L_1 point (which is caused by irradiation and would cause us to overestimate the total spot coverage), we find that some 25% of the visible hemisphere of BV Cen is spotted. This figure is relatively high compared to the spot coverages returned from Doppler images of isolated stars (typically 10 per cent) and is probably due to our less than ideal characterisation of spot filling-factors compared to imaging codes that invoke two-temperature models. However, a visual comparison of BV Cen with the map of AE Aqr (Watson et al. 2006 – for which we estimated had 18% spot coverage) clearly shows that BV Cen has a higher coverage of spots on its surface, and our estimated spot coverage of 25% for BV Cen is consistent with this. Furthermore, a TiO study by Webb et al. (2002) found a 22% spot coverage for the CV SS Cyg, comparable to what we find for BV Cen.

Based on our spot characterisation scheme outlined above, we have determined the distribution of starspots as a function of latitude scaled either by the total surface area of the star, or by the surface area of the latitude strip over which the spot coverage was calculated (see Fig. 11). This shows that the highest spot-filling factor is achieved at polar latitudes, primarily due to the large high-latitude spot centred at $+65^\circ$. We also find that the spot coverage reaches a minimum at intermediate latitudes around $\sim 45^\circ$. This is also

very similar to what was found for AE Aqr (Watson et al. 2006), though the drop in spot coverage at this latitude is far more evident in BV Cen than for AE Aqr.

Fig. 11 also shows clear evidence for a bimodal distribution of starspots with latitude. Our analysis indicates a lower-latitude site of spot emergence around 25° ; indeed the majority of spots seem to form at lower latitudes in BV Cen. In our Roche tomography study of AE Aqr (Watson et al. 2006), we found some evidence for spots at lower latitudes, although this was somewhat uncertain given the low signal-to-noise of those observations. While the BV Cen data has large phase gaps, this time we can be confident that we are seeing spots at lower latitudes. Many of the features described here, such as the off-pole high latitude spot, the bimodal spot distribution and the relative paucity of spots at intermediate latitudes are also seen in Doppler Images of a number of other stars (see the discussion in Watson et al. 2006 and references therein). What is most startling, however, is the great similarity between the maps of AE Aqr presented in Watson et al. (2006), and those of BV Cen presented in this work.

Finally, we have checked whether the features seen in the Roche tomogram are real, or artefacts due to noise. We carried out two further Roche tomography reconstructions, the first only using the odd numbered spectra, and the other using the even numbered spectra. These are both shown in Fig. 12 and, despite the reduction in phase coverage, both maps show the same features. We are therefore confident that the features in the Roche tomogram are not due to noise.

8 A SLINGSHOT PROMINENCE?

In addition to the many starspot signatures that are visible in BV Cen’s trailed spectra (see Fig 3), a curious narrow feature is also evident between phases 0.328 and 0.366 on the blue edge of the profile. This feature appears as a narrow continuation of the main track through the profiles during this block of observations, but lies outside the stellar absorption profile and therefore cannot lie on the stellar surface. Closer inspection of the individual profiles (see Fig. 13) reveals a narrow, weak emission feature in the continuum of 5 LSD profiles. In order to confirm the reality of this feature, we have visually inspected the profiles that were deconvolved from the blue and red spectra separately to see whether they are present in both sets of profiles. Indeed this feature is present (albeit very weakly) in both sets of profiles which makes it unlikely to be due to noise or a systematic effect arising during the LSD process. This feature is also not due to contamination from lunar or solar light during the observations as this would appear as an absorption feature (e.g. Marsden et al. 2005). Furthermore, moon-rise did not occur until at least 2 hours (extending to 4 hours on the final night) after observations of BV Cen were concluded. The fact that the feature is at zero velocity with respect to BV Cen’s systemic velocity of -22 km s^{-1} rules out a ‘terrestrial’ origin, which would be centred at 0 km s^{-1} . We are therefore confident that this feature is real.

Since the emission feature lies outside the stellar line profile, and hence lies off the stellar limb, it can only be attributed to circumstellar material. Solar prominences ap-

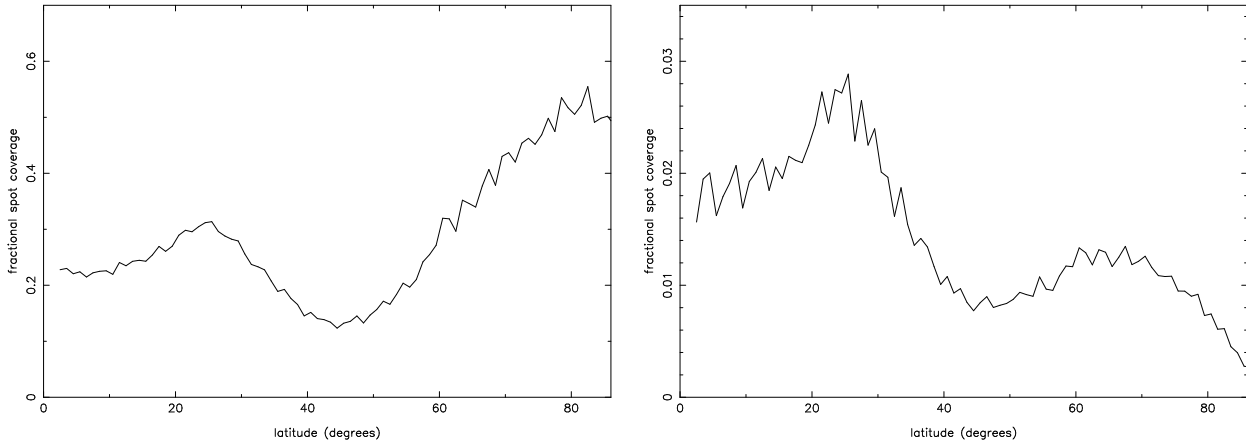


Figure 11. Plots showing the spot coverage on BV Cen as a function of latitude. Left: spot coverage as a function of latitude expressed in terms of the surface area at that latitude. Right: spot coverage as a function of latitude normalised by the total surface area of the northern hemisphere. Since the grid in our Roche tomograms is not aligned along strips of constant latitude, some interpolation between grid elements is required in order to produce these plots. This results in their slightly noisy nature.

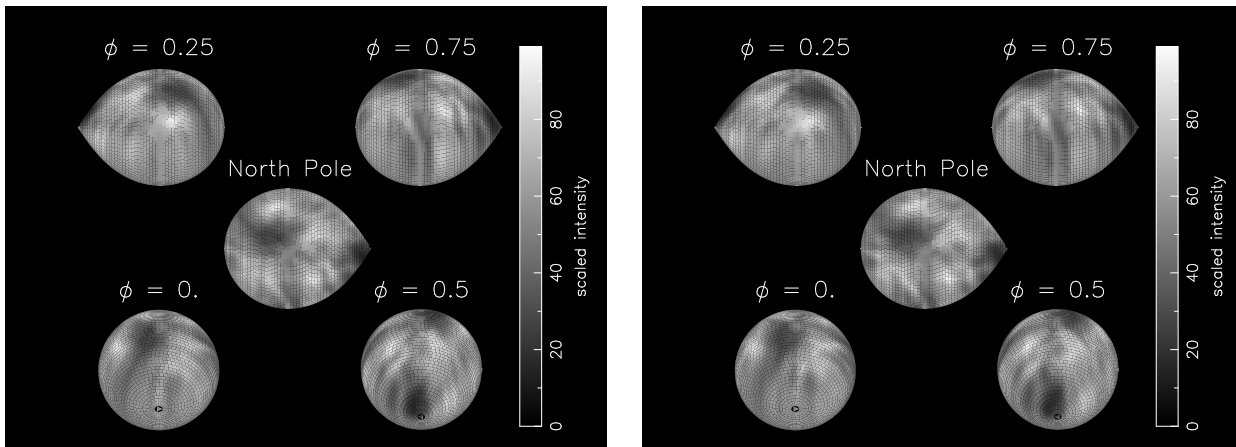


Figure 12. As for Fig. 9, but reconstructions for odd-numbered spectra (left) and even-numbered spectra (right).

pear as bright emission loops when they are viewed off the solar limb, and it is probable that we are also seeing a prominence structure on BV Cen. Indeed, large prominences have been reported on other rapidly rotating stars such as AB Dor (e.g. Cameron & Robinson 1989) and Speedy Mic (Dunstone et al. 2006a) and are often observed as transient absorption features passing through the Doppler broadened $H\alpha$ stellar line. Recently, however, analysis of VLT data of Speedy Mic by Dunstone et al. (2006b) has revealed rotationally modulated emission outside of the stellar $H\alpha$ line due to loops of emission seen off of the stellar disc, but which can also be associated with prominences seen to transit the stellar disc at other times. In addition, peculiar low-velocity emission features seen in SS Cyg and IP Peg during outburst have also been interpreted as ‘slingshot prominences’ (Steeghs et al. 1996). Gaensicke et al. (1998) discovered the presence of highly-ionized low velocity-dispersion material located between the L_1 point and the centre of mass in AM Her which they attributed to a slingshot prominence. Similarly, triple-peaked $H\alpha$ lines following the motion of the donor star in AM Her has been reported by Kafka et al. (2005) and Kafka, Honeycutt & Howell (2006). The authors

interpreted these as long-lived prominences on the donor star and noted that one component was consistent with stellar activity lying vertically above the L_1 point.

The emission feature we see in BV Cen appears stationary at ~ 0 km s^{-1} within the binary frame. This is in keeping with the stationary slingshot prominences seen in SS Cyg and IP Peg by Steeghs et al. (1996), and the low-velocity emission observed in other CVs (Marsh & Horne 1990). Generally, we would expect the emission from prominences observed off the stellar limb to be weak and undetectable for CVs given their faintness. However, it is possible that the prominences are illuminated by the accretion light, causing prominences forming between the donor star and the white dwarf to become visible when otherwise they would be undetectable. Certainly, the low velocity of the emission suggests a position close to the centre-of-mass of the binary at a point between the donor star and white dwarf where such illumination is most likely.

Given that prominences are normally only seen in lines that form above the photosphere (e.g. the Hydrogen Balmer lines), observing them in the LSD profiles which are obtained from photospheric lines is unexpected under normal condi-

tions. We believe that the emission seen in BV Cen’s photospheric lines is due to excitation of these species within low density gas in the prominence due to the impact of irradiation. Thus, we suspect that not only does irradiation cause the prominence to become highly visible, but also causes it to be observable in some photospheric lines in which prominences in a normal, unirradiated environment would not normally emit. We have considered that the emission could be due to a wind launched from the accretion regions. Such a wind, however, would exhibit a radial velocity modulation due to the orbital motion of the primary star which we do not observe. Furthermore, presumably the velocities of material in such a wind would produce a far broader emission line than observed in BV Cen. For these reasons, and the fact that it kinematically matches previous observations of slingshot prominences in CVs, we prefer the interpretation that this feature is the result of an irradiated prominence.

8.1 Limits on the prominence size and height

We find that the emission feature in BV Cen is very narrow, with a velocity width (ΔV) of $\sim 10 \text{ km s}^{-1}$. Using this width we can place an upper limit on the emission source size, l . Following Steeghs et al. (1996), we assume the prominence is co-rotating with the secondary star, so we can write,

$$\frac{\Delta V}{K_1 + K_2} = \frac{l}{a}, \quad (4)$$

where K_1 and K_2 are the radial velocity amplitudes of the white dwarf and donor star, respectively, and a is the orbital separation. For the parameters derived for BV Cen in Section 6, this places an upper limit of 75,000 km. Naturally, the velocity dispersion is increased by instrumental resolution, thermal broadening, saturation broadening and turbulence within the prominence itself. For a 10,000 K prominence the thermal Doppler velocity of Hydrogen is 12.9 km s^{-1} (e.g. Dunstone et al. 2006b). Since the lines included in our LSD are mainly heavier elements such as Fe and Ca, the thermal broadening will be far smaller at $\sim 2 \text{ km s}^{-1}$. Solar prominences exhibit turbulent motions of several km s^{-1} , and Dunstone et al. (2006b) estimate a turbulent velocity of 5 km s^{-1} for the prominences observed on Speedy Mic. However, the dominant broadening mechanism is the $\sim 9.5 \text{ km s}^{-1}$ instrumental resolution of our observations. Considering these limitations, our estimated maximum source size of 75,000 km should be viewed with caution as it is possible that the source is actually unresolved.

We have further analysed the LSD profiles to check whether or not we can see the zero-velocity prominence as it tracks across the stellar disc. We were unable to positively identify any feature with zero-velocity between phases 0.374–0.522 during the first night’s data. This may be due to the large emission bump feature that traverses the profile due to irradiation and/or starspots (see Section 7) which probably masks the prominence itself. Analysis of the second night’s data, however, does reveal a narrow emission bump at zero-velocity between orbital phases 1.974–2.058. This is quite conspicuous (see Fig. 13) as the emission feature moves across the profile in the opposite direction to the starspot features, and Roche Tomography is clearly unable to fit it. This agrees with the picture of a prominence holding material near the centre-of-mass of the binary, and that at

orbital phase ~ 0 we are effectively looking over the top (or possibly under the bottom) of the star at the prominence on the other side. This, therefore, means that the prominence structure must be raised above or below the orbital plane in order for it not to be eclipsed by the donor star at this phase.

Given the lack of eclipse and the parameters found for BV Cen in Section 6, combined with the assumption that the prominence is located above the centre-of-mass of the binary (the point of zero-velocity), we find that the prominence must lie at least 160,000 km above the orbital plane. If we assume that the prominence lies below the centre-of-mass (i.e. we are looking ‘underneath’ the star around phase 0) then it lies out of the orbital plane by at least 2,400,000 km. We feel that this latter case is highly unlikely. First, a prominence below the orbital plane is far more likely to be eclipsed by the accretion regions around orbital phase ~ 0.35 , when it is clearly seen in the data. Second, if we assume that the prominence is only visible due to illumination from the accretion regions then a prominence below the orbital plane is located too far away from the irradiating source.

8.2 Prominence evolution and structure

Three nights of consecutive (albeit interrupted) observations allows a limited discussion of the evolution of the slingshot prominence observed on BV Cen. The prominence is certainly seen at the start of the first night ($\phi = 0.328\text{--}0.366$) before it transits the stellar disc, where it then becomes invisible. We have assumed that, rather than the prominence disappearing at this point, its signature is lost in the complex structure present in the stellar line profile. We are able to pick up an emission feature with the same position in velocity space again at the start of the second night ($\phi = 1.974\text{--}2.038$, see Fig. 13).

Curiously, this prominence feature then disappears after orbital phase 2.038. Since, unlike the first night, the prominence on the second night appears quite clearly in the middle of the stellar line profile it is, on this occasion, difficult to explain how the feature could suddenly be lost within the stellar line. This suggests that the disappearance may be due to rapid evolution of the prominence itself. Indeed, it does seem as though the emission feature weakens during the second night before its apparent disappearance (see Fig. 13). Though the interpretation of a prominence rapidly evolving on timescales of hours is speculative, Dunstone et al. (2006b) also find evidence of individual prominences evolving on timescales of ~ 9 hours on Speedy Mic. Certainly, we can find no evidence for the prominence feature on the 3rd night. This is despite the fact that the emission should be well separated from the stellar line profile after orbital phase 3.645. This supports the idea that the prominence material is not long-lived, only lasting a couple of days before either draining back to the stellar surface or being ejected. Dunstone et al. (2006a) found that, while some prominences on Speedy Mic were still visible after 5 nights, others formed or disappeared over the course of one night.

Finally, unlike the prominences seen on Speedy Mic and AB Dor which lie typically between 2 to 9 stellar radii from the stellar rotation axis (with a concentration at the co-rotation radius), the feature observed in BV Cen is far closer to the stellar surface. If the prominence is located above the

centre-of-mass of the binary, then this places it just $1.5 R_*$ (assuming the Roche-lobe volume radius for BV Cen) from the rotation axis of the secondary star. Although this is at odds with most $H\alpha$ observations which show prominences at or beyond the co-rotation radius, clouds substantially closer to the stellar surface have been reported in HK Aqr (Byrne, Eibe & Rolleston 1996 reported prominences $0.34 - 3.2 R_*$ above the stellar surface) and RE J1816+542 (heights as low as $0.88 R_*$, Eibe 1998).

The height of the prominence feature seen in BV Cen also agrees with X-ray observations of rapidly-rotating isolated stars, even when $H\alpha$ observations of prominences of the stars in question reveal high cloud heights. For instance, in Chandra X-ray observations of AB Dor, Hussain et al. (2005) found that a significant fraction of the emission arose from compact regions near the stellar surface with heights of less than $0.3 R_*$, and that the emitting corona does not extend more than $0.75 R_*$ above the stellar surface. Obviously, the formation mechanism of these prominences and active regions necessitates more work. In particular, the apparent preference for ‘slingshot prominences’ observed in CVs to form at low-velocity sites requires satisfactory explanation.

9 DISCUSSION

We have shown that the donor star in BV Cen is highly spotted, the second CV donor for which this has been shown to be the case. Fig. 10 highlights the striking similarities in spot distribution between BV Cen and AE Aqr, despite their quite different binary parameters and spectral types. Although BV Cen has a higher spot coverage and more low-latitude spots than AE Aqr, both show a high latitude spot displaced towards the trailing hemisphere. It would be interesting if all donor stars in CVs showed high latitude spots displaced in the same direction. Such a deflection could be the result of the orbital motion of the binary. Since the rotation axis lies outside the donor stars in these binaries, one may expect the play of Coriolis (and/or centrifugal) forces on magnetic flux tube emergence to be different from single stars. Further observations, however, are required before we can definitely say that such a deflection of high-latitude spots takes place in CV donors.

Another striking similarity between the two tomograms presented in Fig. 10 is the apparent chain of spots extending down from the polar regions to the L_1 point. This is more evident in the tomogram of AE Aqr, but probably only because there are fewer low latitude features which allows these spots to stand-out more on AE Aqr. We believe that this chain of spots is probably due to the impact of tidal forces due to the close proximity of a compact companion, and such a ‘sub-white dwarf’ concentration of spots is also seen on the pre-CV V471 Tau (Hussain et al. 2006). A concentration of starspots on the inner face of the donor stars in CVs may also have consequences for the accretion dynamics of these objects. It has long been thought that starspots may be able to quench mass-transfer from the donor as they pass across the L_1 point, leading to the low-states seen in many CVs (e.g. Livio & Pringle 1994, King & Cannizzo 1998). Indeed, in their study of the mass-transfer history of AM Her, Hessman, Gänsicke & Mattei (2000) concluded that such a model would require an unusually high spot-coverage near

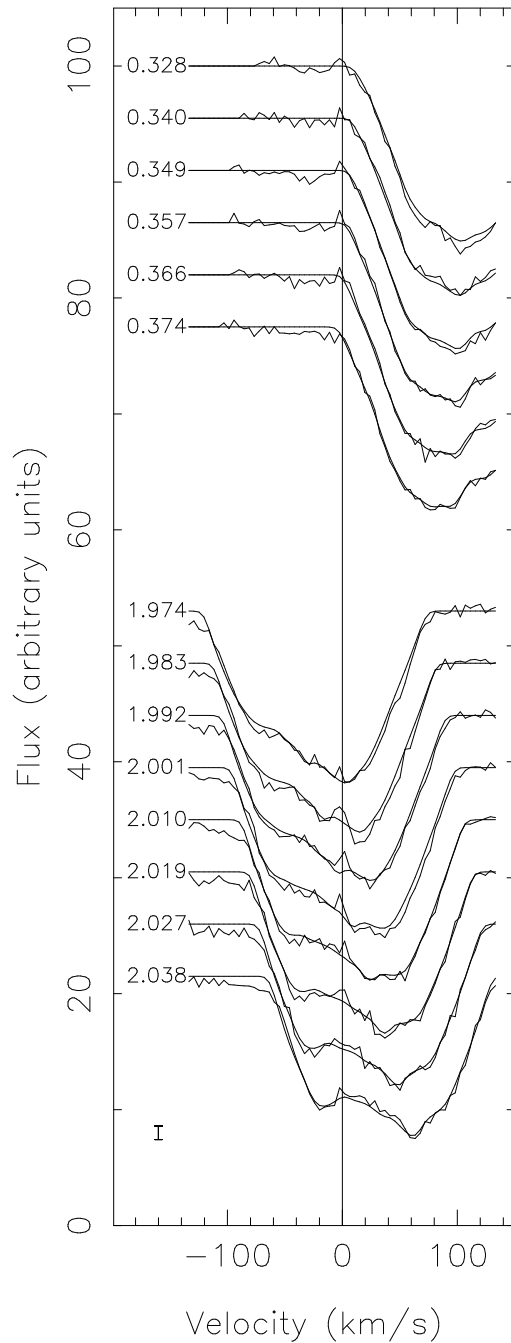


Figure 13. Plots of the LSD profiles that show the narrow emission feature at a velocity of $\sim 0 \text{ km s}^{-1}$ on nights 1 & 2 as discussed in the text. The Roche tomography fits to the data are also plotted and the orbital phase is indicated on the left. Unlike Fig. 2, the orbital motion has not been removed and a vertical line centred on a radial velocity of 0 km s^{-1} has been plotted to show where the emission feature appears. The slingshot prominence feature appears outside of the stellar lines on the first night’s data (top 6 profiles). During the second night (bottom profiles) it appears within the profiles but moves in the opposite direction relative to the starspot features and the Roche tomography code is therefore unable to fit this feature.

the L_1 point, or otherwise some mechanism that drives spots towards the L_1 point. Certainly, both AE Aqr and BV Cen do seem to show increased spot coverages towards the L_1 point in support of their conclusions.

The fact that we see more active regions near the L_1 point may also explain why we appear to see a preference for ‘slingshot prominences’ to form above the donors inner face (Steeghs et al. 1996; Gaensicke et al. 1998; Kafka et al. 2005; Kafka et al. 2006 – and again in this work). Certainly, the fact that prominence material at these locations will be illuminated by the accretion regions also means that observations will be biased towards detecting prominences in the region between the white dwarf and donor star in CVs. Furthermore, if surface magnetic fields are strong enough in the neighbourhood of the L_1 point this may also cause fragmentation of the mass flow, resulting in the inhomogeneous or ‘blobby’ accretion seen in some CVs (e.g. Meintjes 2004; Meintjes & Jurua 2006).

10 CONCLUSIONS

BV Cen is the second CV donor star for which starspots have unambiguously been imaged on. Again, as with AE Aqr, we find a high (25 per cent) spot coverage, and the high activity-level is further confirmed by the detection of a slingshot prominence. Comparison with the Roche tomograms of AE Aqr from Watson et al. (2006) show many similarities between the two systems despite the quite different fundamental parameters of these two binaries. These spot distributions hint at the impact of tidal and/or Coriolis forces on the emergence of magnetic flux tubes in these binaries, and suggest that the inner faces of CV donor stars are unusually heavily spotted. As always, further observations are recommended in order to confirm that such spot distributions are widely seen on CV donors. If a fixed spot distribution were to be found, this would also suggest that differential rotation is suppressed (or at least weak) in CV donors, as suggested by Scharlemann (1982).

ACKNOWLEDGEMENTS

CAW is supported by a PPARC Postdoctoral Fellowship. DS acknowledges a Smithsonian Astrophysical Observatory Clay Fellowship as well as support through NASA GO grant NNG06GC05G. TS acknowledges support from the Spanish Ministry of Science and Technology under the programme Ramón y Cajal. The authors acknowledge the use of the computational facilities at Sheffield provided by the Starlink Project, which is run by CCLRC on behalf of PPARC. The Starlink package PHOTOM was used in this work. We would like to thank the Observatories of the Carnegie Institution of Washington for generously allowing us the use of the Henrietta Swope telescopes at Las Campanas Observatory. The 6.5m Landon Clay (Magellan II) telescope at Las Campanas is operated by the Magellan consortium consisting of the Carnegie Institution of Washington, Harvard University, MIT, the University of Michigan, and the University of Arizona.

REFERENCES

- Ak T., Ozkan M. T., Mattei J. A., 2001, *A&A*, 369, 882
 Barnes J. R., 1999, PhD thesis, University of St. Andrews
 Barnes J. R., Collier Cameron A., James D., Donati J.-F., 2000, *MNRAS*, 314, 162
 Barnes J. R., Collier Cameron A., James D., Donati J.-F., 2001, *MNRAS*, 324, 231
 Barnes J. R., Collier Cameron A., Unruh Y. C., Donati J. F., Hussain G. A. J., 1998, *MNRAS*, 299, 904
 Barnes J. R., Lister T., Hilditch R., Collier Cameron A., 2004, *MNRAS*, 348, 1321
 Bernstein R., Sheckman S. A., Gunnels S. M., Mochneck S., Athey A. E., 2003, in Iye M., Moorwood A. F. M., eds, *Instrument Design and Performance for Optical/Infrared Ground-based Telescopes*. Edited by Iye, Masanori; Moorwood, Alan F. M. *Proceedings of the SPIE*, Volume 4841, pp. 1694-1704 (2003). MIKE: A Double Echelle Spectrograph for the Magellan Telescopes at Las Campanas Observatory. pp 1694–1704
 Bianchini A., 1990, *AJ*, 99, 1941
 Biazzo K., Frasca A., Catalano S., Marilli E., Henry G. W., Tàs G., 2006, *Mem. Soc. Astron. Ital. Suppl.*, 9, 220
 Byrne P. B., Eibe M. T., Rolleston W. R. J., 1996, *A&A*, 311, 651
 Cameron A. C., Robinson R. D., 1989, *MNRAS*, 238, 657
 Claret A., 1998, *A&A*, 335, 647
 Collier Cameron A., 1992, in Byrne P. B., Mullan D. J., eds, *Surface Inhomogeneities on Late-type Stars* Springer Verlag, p. 33
 Collier Cameron A., 2001, in Boffin H., Steeghs D., eds, *Astrotomography: Indirect Imaging Methods in Observational Astronomy* Springer-Verlag Lecture Notes in Physics, Berlin, p. 183
 Collier Cameron A., Unruh Y. C., 1994, *MNRAS*, 269, 814
 Dall T. H., Bruntt H., Strassmeier K. G., 2005, *A&A*, 444, 573
 Davey S., Smith R. C., 1992, *MNRAS*, 257, 476
 Dhillon V. S., Watson C. A., 2001, in Boffin H., Steeghs D., eds, *Astrotomography: Indirect Imaging Methods in Observational Astronomy* Springer-Verlag Lecture Notes in Physics, Berlin, p. 94
 Donati J.-F., Semel M., Carter B. D., Rees D. E., Collier Cameron A., 1997, *MNRAS*, 291, 658
 Dunstone N. J. and Cameron A. C., Barnes J. R., Jardine M., 2006b, *astro-ph/0610106*
 Dunstone N. J., Barnes J. R., Cameron A. C., Jardine M., 2006a, *MNRAS*, 365, 530
 Eaton N., Draper P. W., Allen A., 2002, *Starlink User Note 45*, PHOTOM – A Photometry Package version 1.9-0. RAL
 Eibe M. T., 1998, *A&A*, 337, 757
 Frasca A., Biazzo K., Catalano S., Marilla S., Rodonò M., 2005, *A&A*, 647, 655
 Gaensicke B. T., Hoard D. W., Beuermann K., Sion E. M., Szkody P., 1998, *A&A*, 338, 933
 Gilliland R. L., 1982, *ApJ*, 263, 302
 Hatzes A. P., Vogt S. S., 1992, *MNRAS*, 258, 387
 Hessman F. V., Gänsicke B. T., Mattei J. A., 2000, *A&A*, 361, 952
 Holzwarth V., Schüssler M., 2003, *A&A*, 405, 303
 Hussain G. A. J., Allende Prieto C., Saar S. H., Still M.,

- 2006, MNRAS, 367, 1699
- Hussain G. A. J., Brickhouse N. S., Dupree A. K., Jardine M. M., van Ballegooven A. A., Hoogerwerf R., Collier Cameron A., Donati J.-F., Favata F., 2005, ApJ, 621, 999
- Jeffers S. V., Barnes J. R., Collier Cameron A., 2002, MNRAS, 331, 666
- Kafka S., Honeycutt R. K., Howell S. B., 2006, AJ, 131, 2673
- Kafka S., Honeycutt R. K., Howell S. B., Harrison T. E., 2005, AJ, 130, 2852
- King A. R., Cannizzo J. K., 1998, ApJ, 499, 348
- Kraft R. P., 1967, ApJ, 150, 551
- Kupka F., Piskunov N. E., Ryabchikova T. A., Stempels H. C., W. W. W., 1999, A&AS, 138, 119
- Kupka F. G., Ryabchikova T. A., Piskunov N. E., Stempels H. C., W. W. W., 2000, Baltic Astronomy, 9, 590
- Lister T., Collier Cameron A., Bartus J., 1999, MNRAS, 307, 685
- Livio M., Pringle J. E., 1994, ApJ, 427, 956
- Marsden S. C., Waite I. A., Carter B. D., Donati J. F., 2005, MNRAS, 359, 711
- Marsh T. R., Horne K., 1990, ApJ, 349, 593
- Meintjes P. J., 2004, MNRAS, 352, 416
- Meintjes P. J., Jura E., 2006, MNRAS, 372, 1279
- Mestel L., 1968, MNRAS, 138, 359
- Morton D. C., 1991, ApJS, 77, 119
- Nordström B., Mayor M., Andersen J., Holmberg J., Pont F., Jorgensen B. R., Olsen E. H., Udry S., Mowlavi N., 2004, A&A, 418, 989
- Politano M., 1996, ApJ, 465, 338
- Rappaport S., Verbunt F., Joss P. C., 1983, ApJ, 275, 713
- Richman H. R., Applegate J. H., Patterson J., 1994, PASP, 106, 1075
- Rutten R. G. M., Dhillon V. S., 1994, A&A, 288, 773
- Rutten R. G. M., Dhillon V. S., 1996, in Evans A., Wood J. H., eds, Cataclysmic Variables and Related Objects Kluwer Academic Publishers, Dordrecht, p. 21
- Samus N. N., Durlevich O. V., et al. 2004, VizieR Online Data Catalog, 2250, 0
- Scharlemann E. T., 1982, ApJ, 253, 298
- Schüssler M., Solanki S. K., 1992, A&A, 355, 1087
- Schwope A. D., Hasinger G., Lehmann I., Schwarz R., Brunner H., Neizvestny S., Ugryumov A., Balega Y., Trümper J., Voges W., 2000, Astron. Nachr., 321, 1
- Schwope A. D., Staude A., Vogel J., Schwarz R., 2004, Astron. Nachr., 3, 197
- Spruit H. C., Ritter H., 1983, A&A, 124, 267
- Steeghs D., Horne K., Marsh T. R., Donati J.-F., 1996, MNRAS, 281, 626
- Strassmeier K. G., Fekel F. C., 1990, A&A, 230, 389
- Thoroughgood T. D., Dhillon V. S., Watson C. A., Buckley D. A. H., Steeghs D., Stevenson M. J., 2004, MNRAS, 353, 1135
- Vogt N., Breysacher J., 1980, ApJ, 235, 945
- Vogt S. S., Penrod G. D., 1983, PASP, 95, 565
- Warner B., 1995, Cataclysmic Variable Stars. Cambridge University Press, Cambridge
- Watson C. A., Dhillon V. S., 2001, MNRAS, 326, 67
- Watson C. A., Dhillon V. S., 2004, Astron. Nachr., 325, 189
- Watson C. A., Dhillon V. S., Rutten R. G. M., Schwope A. D., 2003, MNRAS, 341, 129
- Watson C. A., Dhillon V. S., Shabaz T., 2006, MNRAS, 368, 637
- Webb N. A., Naylor T., Jeffries R. D., 2002, ApJ, 568, 45